**Fracture toughness measurement of thin nanoporous films on stiff substrates**

D.J. Morris,[†] R.F. Cook
*National Institute of Standards and Technology, Gaithersburg, Maryland USA*

*Nanoporous low-dielectric-constant films constitute a class of materials that are plagued by fracture concerns and are not amenable to traditional fracture toughness measurement techniques. An indentation fracture toughness measurement technique has been developed for these materials. The experiment utilizes nanoindentation in combination with cube-corner indenters which create flaws are on the scale of the film thickness, about a micrometer. Interpretation of experimental results are a far-reaching generalization of the traditional Vickers based indentation test used for ceramics at the mesoscale. Cube-corner indentation fracture is dominated by crack-wedging effects that are not important for Vickers indentation. Film-substrate elastic coupling is very important, and is manifested in three distinct ways. After film-substrate coupling phenomena are identified, they are combined with acute indentation fracture models to form a complete thin-film indentation fracture mechanics model. The fracture toughness of two materials have been measured to be 0.09 MPa $m^{1/2}$ and 0.05 MPa $m^{1/2}$.*

**Variables**

| | |
|---|---|
| $a$ | contact radius |
| $c$ | surface crack length |
| $c'$ | crack depth |
| $\bar{E}$ | plane-strain elastic modulus |
| $G$ | mechanical energy release rate (MERR) |
| $H$ | hardness |
| $K$ | stress-intensity factor (SIF) |
| $\ell$ | Crack aspect ratio |
| $P$ | indentation load |
| $R$ | fracture resistance |
| $s$ | Zak-Williams stress-singularity exponent |
| $t$ | film thickness |
| $T$ | fracture toughness |
| $W$ | wedginess |
| $\alpha$ | Dundurs elastic mismatch parameter (1 of 2) |
| $\beta$ | Dundurs elastic mismatch parameter (2 of 2) |
| $\psi$ | channel crack geometry factor |
| $\phi$ | indenter axis-to-face angle |
| $\sigma$ | film stress |
| $\chi$ | SIF amplitude |
| $\nu$ | Poisson's ratio |
| $\mu$ | shear modulus |

**Super- and sub-scripts**

| | |
|---|---|
| A | apparent |
| CH | channel crack |
| C | contact |
| F | film |
| I | indentation |
| PC | partially-cracked |
| S | substrate |
| TH | threshold |
| W | wedging |

[†] Corresponding author. dylan.morris@nist.gov

## 1 Introduction

Indentation is widely used to locally probe elastic modulus, hardness [1], viscoelastic and creep properties [2], and interfacial fracture (adhesion) [3]. Yet quantitative measurements of the fracture toughness of thin films remain difficult, despite considerable effort in the contact and fracture community. The fracture toughness of some thin films adhered to silicon have been found by consideration of the equilibrium crack spacing under uniform tension, induced by bending of the substrate [4]. This technique relies on sufficient strain transfer from the substrate to the film (by strain match at the interface), implying that film cannot be too compliant relative to the substrate. Other attempts at measurement of the fracture properties in small volumes rely on microfabrication of special structures [5-7].

It is therefore desirable to develop a fracture toughness measurement method that uses a mechanical probe, with little or no special specimen preparation. This is why indentation fracture toughness estimation [8] has garnered so much attention. Indentation by a sphere, or a sharp Vickers diamond is typically used for brittle glasses and ceramics. Sharp indentation has the advantage that it nucleates its own flaws, which obviates the need for pre-existing surface flaws (as would be needed in Hertzian – cone-cracking toughness estimates, e.g. [9]). The hurdle, then, is nucleation of a crack. While the commonly used Vickers probe cannot nucleate radial cracks at the ≈ micrometer-scale needed to study ≈ micrometer-scale features, a much more acute probe, such as the corner of a cube, can. [10]

To this end, the indentation fracture toughness technique has been extended to thin films, situated on a substrate that is relatively stiffer and tougher. The materials of interest in this work are low-dielectric (low-$\kappa$) thin films. Recent work [11] has shown that the indentation fracture response (IFR, the relationship of the surface crack length to the indentation load) for low-$\kappa$ films followed no clear scaling relationships, and that the thickness of the film played a very strong role. All of the fracture data could be reconciled (meaning, one value of fracture toughness could be used in modeling all indentation fracture data from one material) by incorporation of substrate effects.

Here, the indentation fracture theory and cube-corner indentation results are briefly reviewed. Then, the IFRs of two other sharp probes on the same films are presented and compared to the cube-corner IFR. These other probes are less acute than the cube-corner, but more acute than the Berkovich indenter. The implications for fracture toughness measurement are then discussed.

## 2 Indentation fracture at the micro- and nano-scale

In small-force instrumented indentation (nanoindentation), the Berkovich probe geometry is commonly used. The Berkovich is a three-sided pyramid with an axis-to-face angle of 65.3°. The Berkovich and the four-sided pyramidal Vickers

are both equivalent to the axisymmetric equivalent indenter (the right cone with the same depth-to-displaced volume or projected-area-to-contact-radius relationship) of axis-to-conical-surface angle of 70.3°. This simplification is frequently invoked in theoretical and numerical modeling, as it reduces a three-dimensional problem to a two-dimensional problem. The essential equivalence between the Vickers and Berkovich geometries in the context of indentation fracture has been shown [12].

However, it has also been shown that for the cube-corner geometry, the probe drives fracture by wedging the cracks apart [13], instead of driving fracture by residual stresses caused by plastic deformation gradients. As in Hertzian cone cracking, the driving force for fracture is only present when the indenter is pressing on the material. But, as in traditional sharp (for example, Vickers) indentation fracture, the indenter is able to nucleate flaws from the plastic deformation at the contact site. In fact, indentation wedging has been observed with a Vickers indenter in fused silica [14]; the residual indentation stresses in that material are evidently so small that the wedging effect was dominant.

The wedging phenomenon is fortuitous, as the materials under test have a great deal of free volume and are unlikely to store residual stress as a consequence of the plastic deformation. (Indentation residual stresses are considered separately from blanket film residual stresses). Figure 1 is a representative scanning-electron micrograph of a cube-corner indentation in a low–$\kappa$ film. Well-formed radial cracks of length $c$ can be seen.

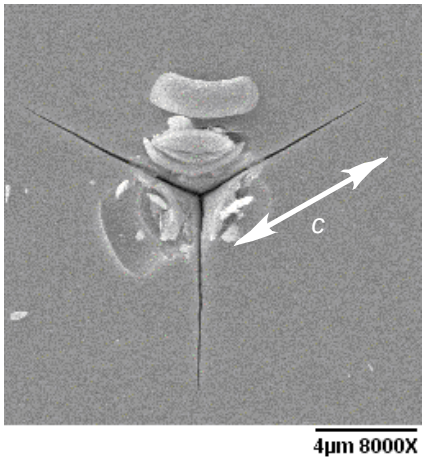


**Figure 1.** Scanning electron image of a cube-corner indentation on a low-$k$ film. The crack length $c$ is shown.

The total elastic stress field of the indenter is the sum of two characteristic fields: contact and wedging. The contact field is that characteristic of the frictionless linear elastic contact solution. While the particulars of the interior stress field depend on the pressure distribution at the surface, at a little distance from the contacted zone the stress fields are essentially that of the Boussinesq point-load stress field, with stresses that fall away as the squared reciprocal of distance. The full-field analytical solutions of the Boussinesq field may then be used to estimate the SIFs of the contact stress field. Radial, surface located cracks are suppressed by the contact's compressive hoop stresses.

The wedging stress field is a consequence of plastic deformation in the contact zone, but it is not residual stress induced by plastic deformation gradients. The surface of the probe, not being parallel to the original surface of the deformed material, imposes dipole forces oriented in the plane of the original surface. These forces induce a stress field that is now hoop-tensile at the surface, which is the

wedging stress field. The wedging field is of shorter range, falling away as the cubed reciprocal of distance, which is characteristic of the stress field of a misfitting inclusion, as it imposes no net force on the indented body [15, 16]. The total action of the indenter is the sum of SIFs for both contact and wedging fields [17]

$$K_{\mathrm{PC}}^{\mathrm{I}} = K_{\mathrm{PC}}^{\mathrm{W}} + K_{\mathrm{PC}}^{\mathrm{C}} = \frac{P}{c^{3/2}}\left[\chi_{\mathrm{PC}}^{\mathrm{W}} + \chi_{\mathrm{PC}}^{\mathrm{C}} \ln\left(2c/a\right)\right]. \tag{2.1}$$

It as been suggested experimentally [14] and theoretically [18] that $\chi^{\mathrm{W}}$ and $\chi^{\mathrm{C}}$ are both strong functions of Poisson's ratio; but, the ratio of the two is effectively independent of Poisson's ratio and is dependent on probe acuity to good approximation. This ratio is the wedginess,

$$W\left(\phi\right) = -\chi^{\mathrm{W}}\left(\phi,\nu\right)/\chi^{\mathrm{C}}\left(\phi,\nu\right) \cong 1.8\cot\left(\phi\right) \tag{2.2}$$

where the factor of 1.8 was found from the experimental determination of *W* for the cube-corner [13] and a scaling analysis [18].

## 3 Film stress

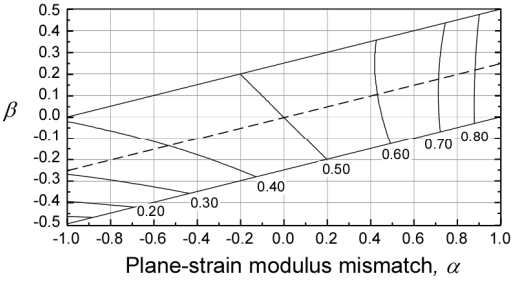


**Figure 2**. *s* in the $\alpha$, $\beta$ plane, within the parallelogram defined by $0 < \nu < 0.5$.

The SIFs for a cracked film, under uniform tensile stress and bonded to a rigid, infinitely thick substrate, were first considered in detail by Beuth [19]. These results were then extended later to elastic-plastic substrates [20] and elastic substrates with finite thickness [21]; however these more complicated analyses are not needed here. A simplified equation [22] derived from Beuth [19] for the SIF of a surface-located crack propagating towards the interface is

$$K_{\mathrm{PC}}^{\mathrm{F}} = 1.987\sigma t^{1/2}\left(\frac{c'}{t}\right)^{1/2}\left(1-\frac{c'}{t}\right)^{1/2-s}. \tag{3.1}$$

*s* is the Zak-Williams stress singularity exponent [23], and is a function of the Dundurs elastic mismatch parameters $\alpha$ and $\beta$ [24], which characterize the elastic mismatch between film and substrate

$$\alpha = \frac{\bar{E}^{\mathrm{F}} - \bar{E}^{\mathrm{S}}}{\bar{E}^{\mathrm{F}} + \bar{E}^{\mathrm{S}}};\ \beta = \frac{\mu^{\mathrm{F}}\left(1-2\nu^{\mathrm{S}}\right) - \mu^{\mathrm{S}}\left(1-2\nu^{\mathrm{F}}\right)}{2\mu^{\mathrm{F}}\left(1-\nu^{\mathrm{S}}\right) + 2\mu^{\mathrm{S}}\left(1-\nu^{\mathrm{F}}\right)}. \tag{3.2}$$

$\alpha$ is a measure of plane-strain modulus mismatch, and $\beta$ is related to differences in compressibility. For each $\alpha$, $\beta$ pair there is a corresponding *s* that characterizes the strength and shape of the film stress SIF [23]. Figure 2 is a map of *s* on the $\alpha$, $\beta$ plane. Also shown is a parallelogram, enclosing all combinations of Poisson's ratio such that $0 \le \nu \le 0.5$ [24]. When there is no elastic mismatch, $s = 0.5$. In the limit $\bar{E}^{\mathrm{F}} << \bar{E}^{\mathrm{S}}$ and $\nu^{\mathrm{F}} \approx 0$, then $s \approx 0$.

One recognizes that, if $s$ = ½, then Equation (3.1) is reduced to the SIF for a plane-strain crack propagating under the influence of uniform stress. Deviations of $s$ from ½ characterize distortions in the SIF as the crack approaches the substrate. For $s$ < ½, $K_{\mathrm{PC}}^{\mathrm{F}} = 0$ when the crack tip just reaches the interface. Therefore, $K_{\mathrm{PC}}^{\mathrm{F}}$ has a maximum within the film. For $s \approx 0$, this maximum in the middle of the film at $c'/t^{\mathrm{F}} = 1/2$.

## 4 Substrate attenuation

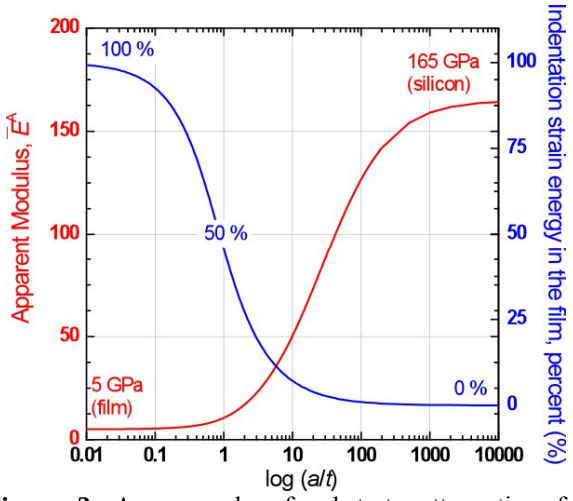


**Figure 3**. An example of substrate attenuation for indentation of a compliant film ($E$ = 5 GPa) on a silicon substrate ($E$ = 165 GPa).

A common problem in nanoindentation is the estimation of the plane-strain modulus of a film, $\bar{E}^{\mathrm{F}}$, on a substrate with significant elastic mismatch. To this end, many theories have been developed that relate the apparent modulus $\bar{E}^{\mathrm{A}}$ (that perceived by appropriate analysis) as some combination of the film and the substrate. As the indenter penetrates more deeply into the film, the relative contribution of the substrate becomes greater. Then, with an appropriate model, e.g. [25, 26] and knowledge of the properties of the substrate, apparent moduli may be extrapolated to zero penetration depth.

The consequence of film-substrate elastic mismatch on indentation fracture SIFs must also be taken into account. Departure of $\bar{E}^{\mathrm{A}}$ from $\bar{E}^{\mathrm{F}}$ indicates that strain energy is being partitioned between film and substrate. The strain energy that has been lost to the substrate (which, may be thought of as constraint on the development of strain in the film) is unavailable to drive fracture. Figure 3 is a demonstration of the variation of apparent modulus $\bar{E}^{\mathrm{A}}$ and the fraction of strain energy contained in the film with equations previously developed [22] for a hypothetical $\bar{E}^{\mathrm{F}} = 5$ GPa low-$\kappa$ film on silicon ($\bar{E}$ = 165 GPa). This shows that in the rigid substrate limit, the fraction of strain energy in the film varied as $\bar{E}^{\mathrm{F}}/\bar{E}^{\mathrm{A}}$. As shown in Figure 3, the strain energy in the film has been halved when $\bar{E}^{\mathrm{A}}$ is ≈ 10 GPa, which is still very far removed from the properties of the substrate. In dynamic nanoindentation [27] the modulus is monitored during indentation and therefore $\bar{E}^{\mathrm{F}}/\bar{E}^{\mathrm{A}}$ is known as a function of load. Then, $K^{\mathrm{I}}$ is attenuated by $\bar{E}^{\mathrm{F}}/\bar{E}^{\mathrm{A}}$. The substrate attenuation correction can be as large as 60 % [22].

## 5 Fracture toughness measurement with a cube-corner

With all SIFs identified, the fracture equilibrium equation for the partially-cracked film is [22]

$$\frac{\bar{E}^{\mathrm{F}}}{\bar{E}^{\mathrm{A}}}\frac{P}{c^{3/2}}\left[1-\ln\left(2c/a\right)/W\right]=\frac{T}{\chi_{\mathrm{PC}}^{\mathrm{W}}}-1.987\frac{\sigma}{\chi_{\mathrm{PC}}^{\mathrm{W}}}t^{1/2}\left(\frac{\ell c}{t}\right)^{1/2}\left(1-\frac{\ell c}{t}\right)^{1/2-s}. \quad (5.1)$$

The left side is the attenuated $K^{\mathrm{I}}$, and the right side is the combined action of film toughness and film stress. The quantities $\ell$, $\left(T/\chi_{\mathrm{PC}}^{\mathrm{W}}\right)$ and $\left(\sigma/\chi_{\mathrm{PC}}^{\mathrm{W}}\right)$ are found from least-squares minimization. The unknown $\chi_{\mathrm{PC}}^{\mathrm{W}}$ is then eliminated by independent measure of the film stress to estimate $T$. Two types of low-$\kappa$ films (Type I and II; dielectric and mechanical properties are in Table I) were tested. As an example, the fracture data are shown in Figure 4a for Type I low-$\kappa$ film. The vertical dashed lines correspond to 150 % of the film thickness, as a surface crack length twice the film thickness has probably developed into the channeling geometry [28]. The minima in the attenuated $K^{\mathrm{I}}$ are indicative of the maximum in $K_{\mathrm{PC}}^{\mathrm{F}}$ for a compliant film ($s < ½$).

TABLE I. Electromechanical properties and thickness of low- $\kappa$ films.

| Material | $\kappa$ | $t$ (μm) | $\sigma$ (MPa) | $H^{\mathrm{F}}$ (GPa) | $\bar{E}^{\mathrm{F}}$ (GPa) |
|---|---|---|---|---|---|
| Type I | 2.2 | 2.4, 1.6, 1.2 | ≈30 | 0.4 | 3.1 |
| Type II | 2.8 | 2.0, 1.5, 1.0, 0.5 | ≈60 | 1.5 | 9.3 |

Figures 4b plots the experimentally determined IFRs, and IFR simulations for both the partially-cracked and channeling geometries. The simulations numerically solve Equation (5.1), with some assumptions about the evolution of $a$ and $\bar{E}^{\mathrm{F}}/\bar{E}^{\mathrm{A}}$ with indentation load [22]. The results are listed in Table II; film

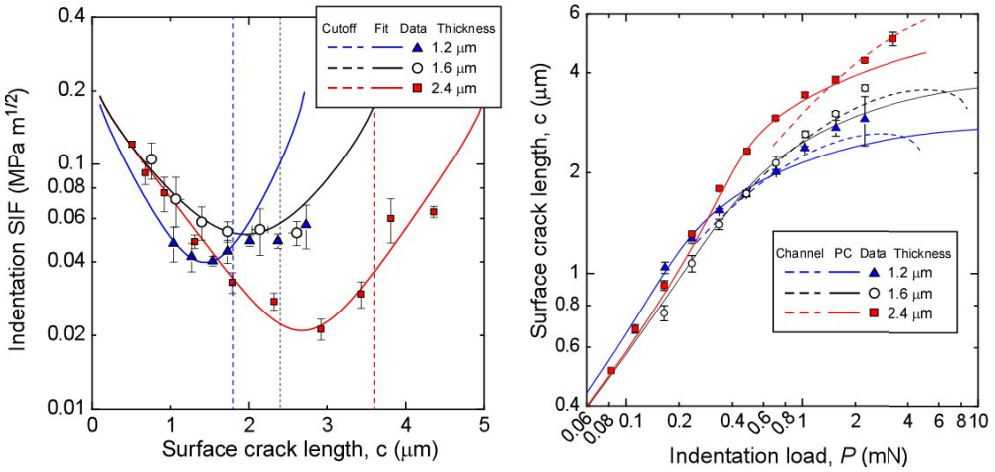


**Figure 4.** Left: (a) fits of Equation (5.1) for Type I film. Right: (b) Experimental data and simulation of crack length vs. load.

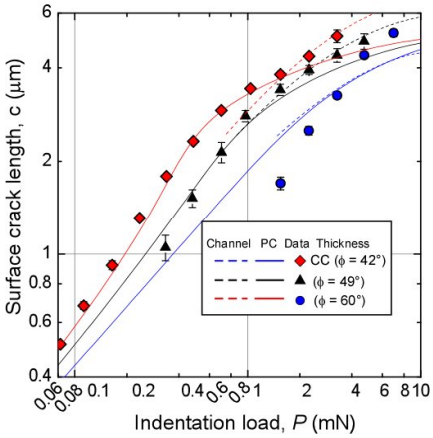


**Figure 5**. IFR (data and simulation) of three probes on 2.4 μm thick Type I low-$\kappa$.

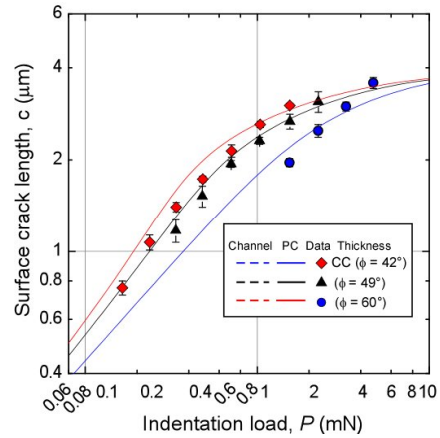


**Figure 6**. IFR (data and simulation) of three probes on 1.6 μm thick Type I low-$\kappa$.

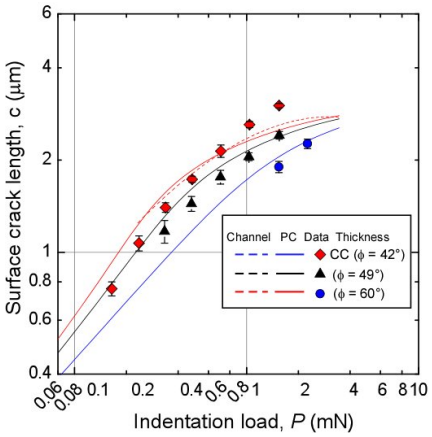


**Figure 7**. IFR (data and simulation) of three probes on 1.2 μm thick Type I low-$\kappa$.

stresses used to calculate the toughness were representative stresses (Table I) provided by the supplier (ISMT). Uncertainty bands listed in Table II correspond to the uncertainty derived from the fitting procedure. The value and uncertainty of toughness are the mean and span of the estimates (one from each thickness).

## 6 Indentation fracture responses of other indenter shapes

As has been previously established, the indenter acuity strongly affects the threshold load for cracking. This, of course, is why the cube-corner is useful for indentation fracture. Unfortunately, the increased damage is not limited to radial cracks; the cube corner is associated with greater plastic deformation and enhancement of competing fracture systems, such as laterals and delamination, reducing the range over which measurements can be made. Less aggressive geometries may also produce satisfactory indentation fracture results in small volumes. Quantitative estimations of toughness from geometries other than the cube-corner awaits experimental measurements of $W$ (and an experimental test of Equation (2.2)). Still, some preliminary conclusions about the efficacy of probes other than the cube corner may be formed by comparison of IFRs of different probes in the same thin film.

Figures 5, 6 and 7 are the experimental and simulated IFRs for Type I material of 2.4 μm, 1.6 μm and 1.2 μm thickness (respectively). Certainly the cube-corner is able to generate more usable data; $P_{TH}$ is small for the more acute probes, but the upper load limit for radial cracking (when spalling and delamination occur) is approximately equal for all probes. The simulations reproduce the experimental data reasonably well, and suggest that there is an approximate upper limit to radial

crack length at $2t^F$, before competing fracture modes interfere with radial cracking.

TABLE II. Low-$\kappa$ film indentation fracture fitting results.

| Material | $t$ (μm) | $T/\chi_{PC}^{W}$ (MPa m$^{1/2}$) | $\sigma/\chi_{PC}^{W}$ (MPa) | $\ell$ | $s$ | $T$ (MPa m$^{1/2}$) |
|---|---|---|---|---|---|---|
| Type I | 2.4 | 0.25 ± 0.01 | 145 ± 6 | 0.48 ± 0.02 | 0.05 | 0.047 ± 0.005 |
| | 1.6 | | 154 ± 8 | 0.42 ± 0.03 | | |
| | 1.2 | | 189 ± 8 | 0.44 ± 0.02 | | |
| Type II | 2.0 | 0.58 ± 0.06 | 366 ± 42 | 0.44 ± 0.05 | 0.12 | 0.087 ± 0.003 |
| | 1.5 | | 395 ± 47 | 0.50 ± 0.01 | | |
| | 1.0 | | 440 ± 59 | 0.57 ± 0.03 | | |
| | 0.5 | | 361 ± 87 | 0.58 ± 0.15 | | |

The threshold indentation loads were remarkably consistent across all three film thicknesses. The threshold load for all film thicknesses are plotted in Figure 8. As $W$ depends linearly on cot $\phi$, we guess that the threshold load is a function

$$P_{TH} = B\left(\cot\phi\right)^n, \tag{5.2}$$

where $B$ is a material (and possibly residual stress [29]) -dependent force, and $n$ characterizes the sensitivity to indenter acuity. The best-fit coefficients are $B = 0.17 \pm 0.01$ mN and $n = -4.0 \pm 0.1$. The exponent $n = -4.0$ is striking in that the threshold load, for fixed indenter acuity, varies as the fourth power of toughness [30].

## 7 Conclusions

The experiment and theory of wedging indentation fracture as applied to thin, brittle, compliant thin films is briefly reviewed. With film stress SIFs appropriate to low-$\kappa$ films on stiff substrates, and indentation SIF attenuation, differing IFRs can be described with one value of $T$. Two films have been tested with cube-corner indentation, and with an estimate of the residual film stresses, the toughness of the films are estimated at approximately 0.09 MPa m$^{1/2}$ and 0.05 MPa m$^{1/2}$.

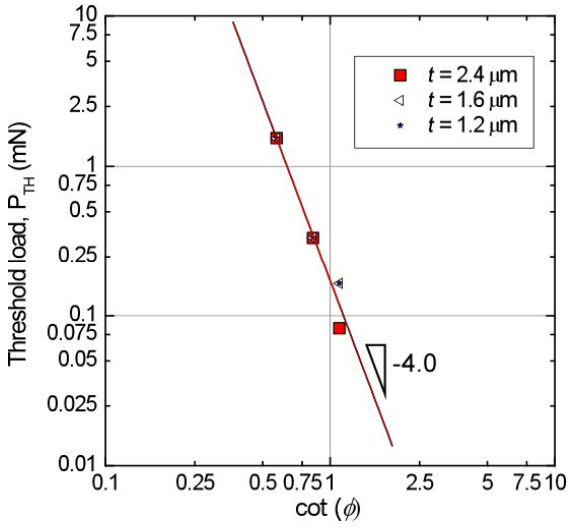


**Figure 8**. Threshold load as a function of cot $\phi$.

Furthermore, the efficacies of indenting probes that are less acute than the cube-corner are explored with regards to low-$\kappa$ indentation fracture. Threshold loads are found to vary as the reciprocal fourth power of cot $\phi$. It is found that the range

over which useful data can be generated is significantly lessened. However, study of the less acute indenters should continue, as they may be better suited to length scales greater than $\cong 1$ μm but less than $\cong 1$ mm, which is the usual scale of a Vickers or Berkovich indentation flaw.

## REFERENCES


[1] W. C. Oliver, G. M. Pharr, Measurement of hardness and elastic modulus by instrumented indentation: Advances in understanding and refinements to methodology, J. Mater. Res., 19 (1) (2004) 3-20.

[2] M. L. Oyen, Analytical techniques for indentation of viscoelastic materials, Phil. Mag., 86 (33-35) (2006) 5625-5641.

[3] M. Kennedy, N. Moody, D. Bahr, The aging of metallic thin films: Delamination, strain relaxation, and diffusion, JOM Journal of the Minerals, Metals and Materials Society, 59 (9) (2007) 50-53.

[4] Q. Ma, Four-point bending technique for studying subcritical crack growth in thin films and at interfaces, J. Mater. Res., 12 (3) (1997) 840-845.

[5] D. Di Maio, S. G. Roberts, Measuring fracture toughness of coatings using focused-ion-beam-machined microbeams, J. Mater. Res., 20 (2) (2005) 299-302.

[6] E. R. Fuller, D. L. Henann, L. Ma, Theta-like specimens for measuring mechanical properties at the small-scale: effects of non-ideal loading, Int. J. Mat. Res., 98 (8) (2007) 729-734.

[7] C. L. Muhlstein, S. B. Brown, R. O. Ritchie, High-cycle fatigue of single-crystal silicon thin films, J. Microelectromech. Syst., 10 (4) (2001) 593-600.

[8] B. R. Lawn, Fracture of Brittle Solids, Cambridge University Press, Cambridge, U.K., 1993.

[9] P. D. Warren, D. A. Hills, S. G. Roberts, Surface flaw distributions in brittle materials and Hertzian fracture, J. Mater. Res., 9 (12) (1994) 3194-3202.

[10] G. M. Pharr, D. S. Harding, W. C. Oliver, Measurement of fracture toughness in thin films and small volumes using nanoindentation methods, in: M. Nastasi, D. M. Parkin, H. Gleiter (Eds.), NATO ASI - Mechanical Properties and Deformation Behavior of Materials Having Ultra-Fine Microstructures, NATO ASI, 1993, pp.449-461

[11] D. J. Morris, R. F. Cook, Indentation fracture of low-dielectric constant films: Part I. Experiments and observations, J. Mater. Res., 23 (9) (2008) 2429-2442.

[12] R. D. Dukino, M. V. Swain, Comparative measurement of indentation fracture toughness with Berkovich and Vickers indenters, J. Am. Cer. Soc., 75 (12) (1992) 3299-3304.

[13] D. J. Morris, R. F. Cook, In situ cube-corner indentation of soda-lime glass and fused silica, J. Am. Cer. Soc., 87 (8) (2004) 1494-1501.

[14] D. J. Morris, A. M. Vodnick, R. F. Cook, Radial fracture during indentation by acute probes: II, experimental observations of cube-corner and vickers indentation, Int. J. Frac., 136 (1-4) (2005) 265-284.

[15] E. H. Yoffe, Stress fields of radial shear tractions applied to an elastic half-space, Phil. Mag. A, 54 (1) (1986) 115-129.
[16] D. J. Morris, Instrumented indentation contact with sharp probes of varying acuity, in: E. Le Bourhis, D. J. Morris, M. L. Oyen, R. Schwaiger, S. Staedler (Eds.), Proceedings of the Materials Research Society 2007, pp.111-116
[17] B. R. Lawn, A. G. Evans, D. B. Marshall, Elastic/plastic indentation damage in ceramics: The median/radial crack system, J. Am. Cer. Soc., 63 (9-10) (1980) 574-581.
[18] D. J. Morris, R. F. Cook, Radial fracture during indentation by acute probes: I, description by an indentation wedging model, Int. J. Frac., 136 (1-4) (2005) 237-264.
[19] J. L. Beuth, Cracking of thin bonded films in residual tension, Int. J. Solids Struct., 29 (13) (1992) 1657-1675.
[20] J. L. Beuth, N. W. Klingbeil, Cracking of thin films bonded to elastic-plastic substrates, J. Mech. Phys. Sol., 44 (9) (1996) 1411-1428.
[21] J. J. Vlassak, Channel cracking in thin films on substrates of finite thickness, Int. J. Frac., 120 (1-2) (2003) 299-323.
[22] D. J. Morris, R. F. Cook, Indentation fracture of low-dielectric constant films: Part II. Indentation fracture mechanics model, J. Mater. Res., 23 (9) (2008) 2443-2457.
[23] A. R. Zak, M. L. Williams, Crack point singularities at a bi-material interface, J. Appl. Mech., 30 (1963) 142-143.
[24] J. Dundurs, Discussion of edge-bonded dissimilar orthogonal elastic wedges under normal and shear loading, J. Appl. Mech., 36 (1969) 650-652.
[25] A. Perriot, E. Barthel, Elastic contact to a coated half-space: Effective elastic modulus and real penetration, J. Mater. Res., 19 (2) (2004) 600-608.
[26] H. Xu, G. M. Pharr, An improved relation for the effective elastic compliance of a film/substrate system during indentation by a flat cylindrical punch, Scripta Mater., 55 (4) (2006) 315-318.
[27] X. Li, B. Bhushan, A review of nanoindentation continuous stiffness measurement technique and its applications, Mater. Charact., 48 (1) (2002) 11-36.
[28] T. Nakamura, S. M. Kamath, Three-dimensional effects in thin film fracture mechanics, Mech. Mater., 13 (1) (1992) 67-77.
[29] D. J. Morris, S. B. Myers, R. F. Cook, Indentation crack initiation in ion-exchanged aluminosilicate glass, J. Mater. Sci., 39 (2004) 2399-2410.
[30] B. R. Lawn, A. G. Evans, A model for crack initiation in elastic/plastic indentation fields, J. Mater. Sci., 12 (11) (1977) 2195-2199.